Journal of Materials Chemistry A

Two-dimensional Ruthenium Boride: A Dirac Nodal Loop Quantum Electrocatalyst for Efficient Hydrogen Evolution Reaction

Journal:	*Journal of Materials Chemistry A*
Manuscript ID	TA-ART-11-2022-008951.R1
Article Type:	Paper
Date Submitted by the Author:	26-Dec-2022
Complete List of Authors:	Gao, Zhen; Hebei Normal University Ma, Fengxian; Hebei Normal University, Wu, Hongbo; Hebei Normal University Ge, Yongheng; Hunan Normal University Zhu, Ziming; Hunan Normal University Department of Physics , Liu, Ying; Hebei Normal University, Physics Jiao, Yalong; Hebei Normal University, Chen, Zhongfang; University of Puerto Rico, Chemistry

Two-dimensional Ruthenium Boride: A Dirac Nodal Loop Quantum Electrocatalyst for Efficient Hydrogen Evolution Reaction

Zhen Gao,[a] FengxianMa,[a,*] HongboWu,[a] Yongheng Ge, [b] ZimingZhu,[b] Ying Liu [a] Yalong Jiao,[a,*] ZhongfangChen[c,*]

[a] College of Physics, Hebei Key Laboratory of Photophysics Research and Application, Hebei Normal University, Shijiazhuang 050024, China
[b] Key Laboratory of Low-Dimensional Quantum Structures and Quantum Control of Ministry of Education, Department of Physics and Synergetic Innovation Center for Quantum Effects and Applications, Hunan Normal University
[c] Department of Chemistry, University of Puerto Rico, Rio Piedras Campus, San Juan, PR 00931, USA.

*E-mail:
fengxianma@hebtu.edu.cn;
yalong.jiao@hebtu.edu.cn;
zhongfang.chen1@upr.edu

Abstract

Catalysts with high carrier mobility, high activity, and an active basal plane have been highly sought for hydrogen evolution reactions (HER). However, combining these advantages into one single material is a grand challenge. Herein, using first principles computations, we predicted that a two-dimensional (2D) Dirac nodal loop semimetal, namely the RuB_4 monolayer, is promising as a superior catalyst for HER. Our systematic computations showed that the single layer RuB_4 is thermodynamically, dynamically, mechanically, and thermally stable and presents multiple Ru and B sites for HER on the basal plane. The estimated Gibbs free energy for hydrogen adsorption at a Ru site is approaching zero (-8.8meV), suggesting its excellent HER performance. The RuB_4 monolayer is a Dirac nodal loop semimetal with high Fermi velocities, which can accelerate charge transfer between catalysts and reaction intermediates. The RuB_4 monolayer is an auxetic material with an out-of-plane negative Poisson's ratio, implying its novel mechanical property. This work provides an example of using a Dirac nodal loop semimetal for high-performance HER catalysts, which is a promising alternative to the known catalysts with trivial metallic properties.

1. Introduction

Due to the increasing scarcity of fossil fuels and the severe threat of climate change, it is urgent to develop renewable, sustainable, and environment-friendly alternative energies to replace exhaustible resources.[1] Because of its high gravimetric energy density and net-zero emissions, hydrogen (H_2) is believed to be one of the leading options for storing renewable energy.[2-5] Water electrolysis, also known as electrochemical water splitting, is a promising approach to sustainably producing hydrogen,[6, 7] in which $H_2$is generated by the so-called hydrogen evolution reaction (HER) at the cathode. High-performance catalysts for HER must be employed to maximize energy conversion efficiency.[8-13]So far, platinum is the best known HER catalyst;[9] however, the scarcity and high cost seriously limit the large-scale applications of Pt-based catalysts.

Two-dimensional (2D) materials have distinguished themselves as promising high-performance HER catalysts[14] due to the large surface area, a high percentage of exposed atoms, and abundant catalytic sites. Several 2D materials, such as graphene,[15-17] transition metal dichalcogenides (TMDs),[18-22] MXenes family,[23] black phosphorus,[24] metal oxides,[25, 26] have been explored so far. Despite the significant progress, the HER activities still need improvement, and several critical issues still need to be solved. For example, the active sites for HER are mainly located on the edge sites of 2D TMDs, while their basal planes are inert.[27, 28] Additionally, most 2D catalysts only display trivial metallic properties, and their carrier mobility is significantly limited. In this context, developing 2D catalysts with active surface area and novel electronic properties is particularly interesting.

Recently, quantum catalysts with nontrivial band topology have shown their promise for HER. It is recognized that the surface state or linear band dispersion at the Fermi level guarantees high charge-carrier mobility and can boost the charge-transfer kinetics during the catalytic process.[29] Additionally, the topologically protected electronic states are robust against defects and impurity-caused backscattering, facilitating reactions at their surfaces.[30] So far, such materials are primarily found in three dimensions (3D), including 3D Weyl semimetals(*e.g.*, transition metal monopnictides family),[31] 3D Dirac semimetals (*e.g.,* $PtSn_4$ and TiSi),[32, 33] and 3D topological insulators (*e.g.,*Bi_2Se_3),[34] while their 2D counterparts remain scarce.[35] To this end, Liu and coworkers theoretically designed a 2D nodal line semimetal $Cu_2C_2N_4$ sheet with a good HER activity,[36] but the active catalytic sites are at the edges, which limits the HER performance; Wang *et al.*successfully identified a 2D Dirac semimetal WB_4 layer with HER active sites on the basal plane,[37] but the isolated Dirac points exhibit very low carrier densities around the Fermi level, leading to very low efficiency of charge transfer during HER.

The progress mentioned above raised the following question, can we find a 2D HER catalyst featuring both active surface sites and nontrivial band dispersion with high carrier densities? To address this question, through systematic density functional theory (DFT) computations, we explored the feasibility of 2D nodal loop semimetals as HER catalysts. Note that a nodal loop semimetal generally possesses a high density of conduction electrons at the Fermi level, thus allowing high charge-transfer kinetics for the HER process. Our computations identified the 2D RuB_4 monolayer as a

concrete example. The RuB_4 monolayer shows double Dirac points in the band structureand possesses a nodal loop centered around the Γ pointin the first Brillouin zone. The estimated Fermi velocity is as high as $4.98 \times 10^{5}\mathrm{m/s}$, which is about 57% of that in graphene, indicating its excellent transport property. Remarkably, the RuB_4 monolayer yields active surface sites for HER, and the estimated Gibbs free energy at Ru sites displays near-zero values (-8.8 meV), which is better than that of Pt, MoS_2, and WS_2. This work demonstrates that 2D nodal loop semimetals can be a promising platform for developing highly efficient HER catalysts.

2. Computational model and details

Our DFT computations were performed using the Vienna *ab initio* simulation package (VASP),[38] and the projector augmented wave (PAW)[39] method was utilized to describethe ion-electron interactions. The Perdew-Burke-Ernzerhof functional (PBE)[40] within the generalized gradient approximation (GGA) was used throughout our computations. The Hubbard correction with the value U of 3.0 eV[41] was employed to deal with Ru's strongly correlated 4d orbitals.[42] The energy cutoff of the plane waves was set to 400 eV. The structures were fully relaxed until the maximum force on each atom was less than 0.005eV/Å, and the energy convergence criterion in the self-consistent calculations was set to 10^{-5} eV. The $4 \times 4 \times 1$ and $8 \times 8 \times 1$ Monkhorst−Pack *k*-point grids were used for geometry optimizations and self-consistent calculations, respectively. A vacuum slab of at least 20 Å in the *z* direction was adopted to avoid artificial interactions between the neighbouring layers.

The phonon dispersion was calculated using the Phonopy code[43] within the density functional perturbation theory (DFPT).[44] Thermal stabilities were evaluated by *ab initio* molecular dynamics (AIMD) simulations. The strain is defined as $\varepsilon = (a-a_0)/a_0$, where a and a_0 are the lattice constants at strained and strain-free states, respectively. According to this definition, negative and positive ε values indicate compressive and tensile stress, respectively.

The total HER pathway can be written as $H^+ + e^- \rightarrow 1/2H_2$.[45] The Gibbs free energy of hydrogen adsorption, ΔG_{H^*}, is the critical descriptor for hydrogen evolution,[46, 47] which is defined as $\Delta G_{H^*} = \Delta E_H + E_{ZPE} - T\Delta S_H$, where ΔE_H, E_{ZPE}, and ΔS_H are the hydrogen chemisorption energy, the reaction zero-point energy, and the entropy change between the adsorbed state and the gas phase, respectively. As $E_{ZPE} - T\Delta S_H$ = 0.24 eV is a well-established approximation,[45] we simplify the Gibbs free energy as $\Delta G_{H^*} = \Delta E_H + 0.24$.

3. Results and discussion

3.1. Structures and stabilities

The RuB_4 monolayer crystallizes in the Pmma space group, and the optimized lattice parameters are a =7.809 Å and b = 7.624 Å with a thickness of 1.84 Å. The average Ru-B bond length is 2.17 Å, and that for the B-B bond is 1.7 Å. As shown in Fig. 1a, the B atoms of the RuB_4 monolayer form a network composed of 4-membered and 8-membered rings, and each Ru atom is octacoordinated to B atoms, forming Ru©B_8 wheel-like structural motifs.

To characterize the bonding behavior in the structure, we calculated the electron localization function (ELF). As shown in Fig. 1b, electrons are predominately localized between B-B atoms. In contrast, electron localizations are absent between B-Ru atoms, reflecting the covalent bonding states between B atoms and the ionic bonding between B and Ru atoms.

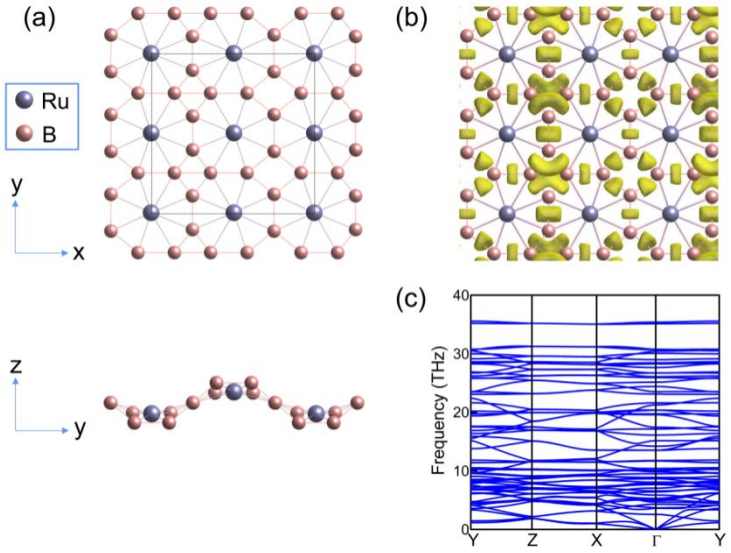

Fig. 1 (a) Atomic structure of the RuB_4 monolayer. The dashed line represents the primitive cell. (b) The electron localization function (ELF), and (c) phonon dispersions of the RuB_4 monolayer. The isosurface for ELF is 0.75 eÅ^{-3}.

To investigate the stabilities of the RuB_4 monolayer, we first calculated its cohesive energy based on the following equation to evaluate its thermodynamic stability:

$$E_{coh} = [E\ (M_xB_y)\ - xE(M) - yE(B)]/(x + y)$$

where x and y represent the number of atoms in the cell, $E(M_xB_y)$ is the total energy of the RuB_4layer, E(M) and E(B) are the energies of isolated Ru and B atoms,

respectively.According to this definition, a more negative E_{coh} value indicates higher thermodynamic stability. The calculated E_{coh} for the RuB_4 monolayer (-7.903 eV/atom) is much lower than that of FeB_2 (-4.87 eV/atom),[48] FeB_3 (-5.93 eV/atom),[49] and FeB_6 (-5.79 eV/atom)[50] monolayers, suggesting the stronger atomic interaction in the RuB_4 monolayer and its good thermodynamic stability.

To evaluate the dynamical stability, we calculated the phonon dispersion (Fig. 1c).As no imaginary modes are available in the entire Brillouin zone, the RuB_4 monolayer is dynamically stable.

Accordingto the elastic stability criteria,[51] a stable 2D square lattice should satisfy $C_{11}, C_{22}, C_{66} > 0$ and $C_{11} + C_{22} - 2C_{12} > 0$, where C_{ij} are the elastic constants. The calculated values (Table S1†) indicate that these mechanical stability criteria are fully satisfied.

At last, we confirmed the thermal stability of the RuB_4 monolayer by performing AIMD simulations at 500 K, 1000K, and 1500 K. At the end of 5 *ps* simulations (Fig. 2), the framework of the RuB_4 sheet is well preserved at the temperature of 500 K. It does not fracture throughout AIMD simulation up to 1500 K. The well-maintained geometries confirm the high thermal stability of the RuB_4 monolayer.

The mechanical properties of the RuB_4 monolayer, including the stress-strain relation, Young's modulus, and the lattice response subject to uniaxial strain, were systematically explored and discussed in the electronic supplementary information (Fig. S1-S5†). Though good mechanical properties, such as high mechanical strength

and negative Poisson's ratio, were found in RuB_4, they are excluded in the following discussion as these are not our primary focus.

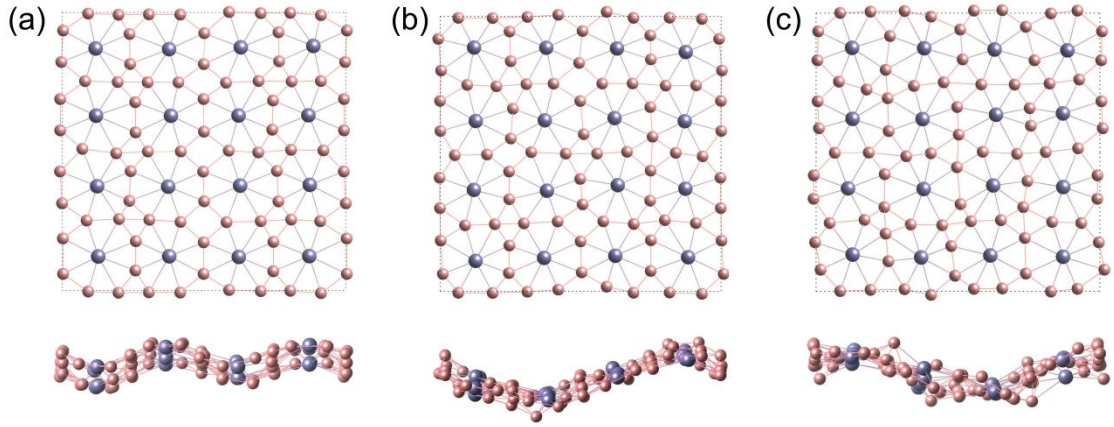

Fig. 2 Snapshots of the RuB_4equilibrium structures at the end of 5 *ps*AIMD simulations at (a) 500 K, (b) 1000 K, and (c) 1500 K.

3.3 Electronic properties

To examine the electronic properties of the RuB_4 sheet, we first calculated the band structure without considering the spin-orbital coupling (SOC) effect. The valence band maximum (VBM) and the conduction band minimum (CBM) touch in the vicinity of the Fermi level (Fig. 3a), leading to a zero bandgap. Interestingly, there are two band crossing points along the Y-Z and Γ-Y lines: Dirac point 1 (DP1) is along the Y-Z line and 24 meV above the Fermi level; in contrast,Dirac point 2 (DP2) is along the Γ-Y line and 55 meV below the Fermi level. The analysis of the density of states (DOS) revealed that the Dirac states are dominantly contributed by the orbitals from Ru atoms and marginally derived from that of B atoms (Fig. 3b).According to the orbital-resolved band structures (Fig. S6†), DP1is mainly contributed by the hybridization of S, p_x, p_z orbitals from B atoms and p_x, p_z, d_{xz}, d_{yz},

$d_{x^2-y^2}$, d_{z^2} orbitals from Ru atoms. In contrast, DP2 is derived from the coupling of p_z orbital of B atoms and s, p_z , d_{yz} ,d_{z^2} orbitals from Ru atoms.

By carefully scanning the band structure in the Brillouin zone, we found that the Dirac points are not isolated; instead,they belong to a nodal loop centered at the Y point (Fig. 3c). This finding was confirmed by plotting the band structures from some selected K point paths, where the Dirac points also exist along the Y-A_1, Y-A_2, and Y-X lines (Fig. S7†).The nodal loop is evident in the 3D band structure for the RuB_4 monolayer (Fig. 3d).

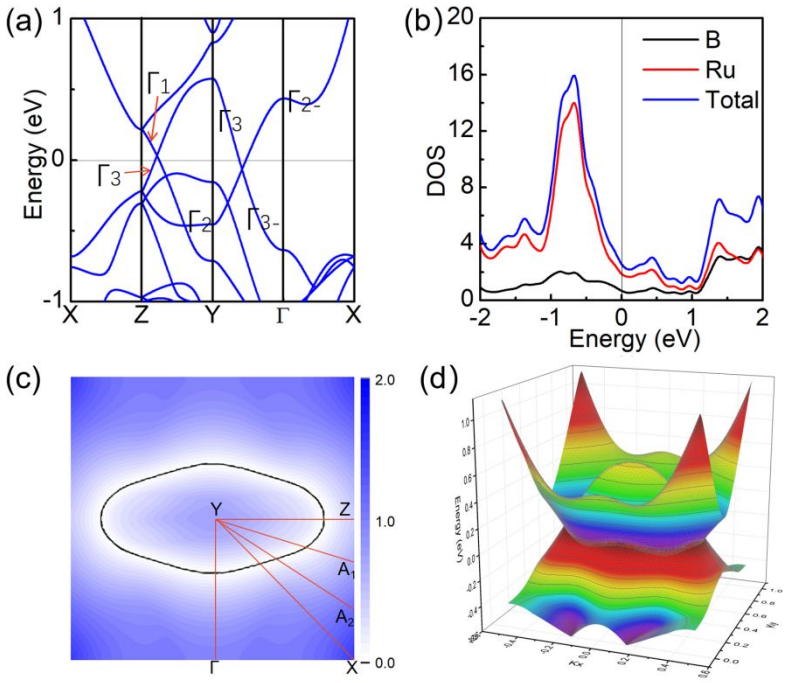

Fig. 3(a) Band structure and (b) density of states (DOS) for the RuB_4 monolayer. The irreducible representations of some selected bands are shown in (a). (c) The shape of the Dirac nodal loop. Some chosen K-point paths are highlighted in red lines. The color map indicates the local gap between two crossing bands. (d) 3D band structure for the RuB_4 monolayer.

To explore the robustness of the nodal loop, we analyzed the symmetry properties of the low-energy bands. It is found that the nodal loop is protected by the glide mirror symmetry M_z, since the holelike band has the M_z eigenvalue $+\mathrm{i}$ while the electronlike band has the opposite M_z eigenvalue $-\mathrm{i}$ (Fig. 3a). Therefore, the electronlike band must cross the holelike band without hybridization. The resulting loop is protected as long as the glide mirror symmetry is maintained.

The symmetry-protected nodal loop can be further confirmed by applying biaxial strains to the RuB_4 sheet, as strains can preserve the structural topology and significantly change the materials' lattice constants. Notably, the Dirac points of the RuB_4 monolayer survive within both positive and negative biaxial strains ranging from -3% to 3% (Fig. S8†).

To explore how the metal electrodes affect the band structure of RuB_4, we take Ni as an example and constructed a model of a RuB_4 monolayer on the Ni (1 0 0) surface. Band structure calculations indicate the whole system displays metallic feature. The multiple Dirac points from RuB_4 can be preserved and they shift slightly below the Fermi level (see Fig. S9† for more details).

Remarkably, the linear band dispersions in the vicinity of the Fermi level indicate that charge carriers in these bands behave as a small mass of Dirac fermions.[52] To examine the carrier mobility of the RuB_4 monolayer, we evaluated the Fermi velocity (υ_F) by linearly fitting the first derivatives of the bands near the Dirac points. Specifically, the expression is $\nu_F = \partial E/(\hbar \partial k)$, where $\partial E/\partial k$ is the slope of the linear dispersions and $\hbar$ is the reduced Planck's constant. The calculated maximum

velocities for the RuB_4 monolayer are $4.32 \times 10^5 \mathrm{m/s}$ and $4.98 \times 10^5 \mathrm{m/s}$, respectively, for DP1 and DP2, which are about 33% - 57% of that in graphene ($1.1 \times 10^6 \mathrm{m/s}$)[53], but larger than many other 2D materials such as single-layer Be_3C_2,[54] TiB_2,[55] and P6/mmm boron sheet.[56] Furthermore, we found that the band structure with SOC displays a small gap opening of 29.4 meV for DP1 and 3.7 meVfor DP2 (Fig. S10†). These values for RuB_4 monolayer are comparable to that in TiB_2 crystal (22 - 33 meV),[57] but much smaller than those of CaAgAs (~73 meV)[58] and ZrSiTe (~73 meV)[59], implying the weak SOC effect in RuB_4.

In general, the symmetry-protected nodal loop and high Fermi velocity endow the RuB_4 sheet with excellent transport properties, which inspired us to investigate its potential application as catalysts for hydrogen evolution reactions.

3.4 Hydrogen evolution reaction catalyzed by the RuB_4 monolayer

For the H adsorption process, we built the model by adsorbing one H atom on the surface of the unit cell of the RuB_4sheet and tested different Ru and B sites. It is found that both B and Ru sites are active for HER. Specifically, the calculated ΔG_{H^*} at the B site is -0.12 eV, while that at the metal Ru site has a near-zero ΔG_{H^*} value of -0.0088 eV, suggesting the excellent HER performance at these Ru sites.

We calculated the charge density difference for an H atom on top of the Ru site to trace the charge transfer during HER. As shown in Fig. 4a, charge accumulation occurs at the bridge site between Ru and H atoms. Quantitatively, Bader charge analysis reveals that the adsorbed H atom has received 0.25e from the nearest Ru

atom. These results indicate that the H atom can capture a sizable charge from the catalytic surface to form H_2, thus facilitating the electrocatalytic process.

The ΔG_{H^*} for the RuB_4 sheet is significantly lower than those in typical 3D Weyl topological catalysts, including NbP, TaAs, and NbAs,[32] and 2D nodal line catalysts such as the $Cu_2C_2N_4$ sheet.[36] To compare the performance of the RuB_4 monolayer with other typical HER catalysts, we plotted the volcano curve (Fig.4b). The ΔG_{H^*} for the RuB_4 monolayer is located at the top of the volcano curve, indicating that the basal plane of RuB_4 is highly active, its performance is even better than that of Pt (ΔG_{H^*}=-0.09 eV).

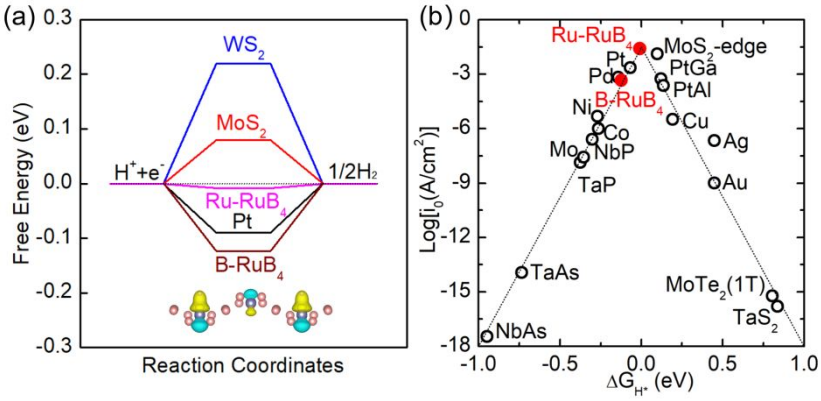

Fig. 4 (a) Gibbs free energy diagram of the HER at different sites of the RuB_4 monolayer at equilibrium potential. Inset: The electron depletion (green) and accumulation (yellow) during the H adsorption. The isosurface is set to be 0.02 eÅ^{-3}. (b) Volcano plot for the HER of the RuB_4 sheet in comparison with various reference materials.

Next, we explored the interplay between the strain effect and the HER performance of the RuB_4 monolayer. Fig. 5a-b show the relevant variation of free energies of hydrogen adsorption under uniaxial strain. For the B sites, the tensile strain drives ΔG_{H^*} toward a more negative value, which could reduce the catalytic performance. Differently, applying a slight compressive strain would induce ΔG_{H^*} shifting toward thermoneutrality, and the strain at -2% can maximally enhance the HER performance of the B sites (ΔG_{H^*}= -98 meV); however, when the sheet is further compressed ($\varepsilon \leq$ -3%), the value of ΔG_{H^*} turns out to be decreasing. For the Ru sites, ΔG_{H^*} rises monotonically with increasing strain. Significantly, when a positive strain of 2% is applied, the ΔG_{H^*} value can be modified to-0.81meV, which is expected to be one of the best values of ΔG_{H^*} reported so far.[32, 45, 60-63] Note that even when the material is stretched by 4%, the ΔG_{H^*} value is still close to zero (5.6 meV). Thus, compared with the B sites, the Ru sites in the RuB_4 sheet have much higher HER activity, which can also be well maintained under external strains.

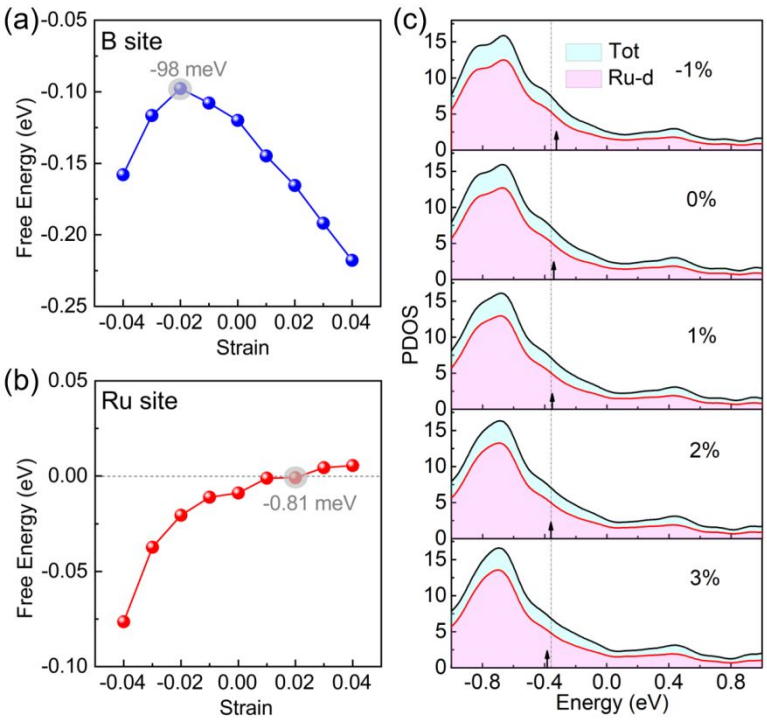

Fig. 5 The calculated Gibbs free energy of hydrogen adsorption (ΔG_{H*}) on the (a) Ru and (b)B sites under strain effect (the adsorption on the Ru site is given in red, while that on the B site is given in blue. (c) The projected density of states for the d orbital of Ru in the strained conditions. The vertical dashed line corresponds to the location of the 2% strained state, which has the highest catalytic activity. Black arrows mark the d-band centers. The energy at the Fermi level was set to zero.

To explore the origin of the superior HER activity in the RuB_4 sheet, we studied the evolution of the d-band centre with the change of strain.When the d-band center is closer to the Fermi level, the resultant anti-bonding orbital increases energy, and its occupancy reduces, corresponding to a more robust H* adsorption.[64] Conversely, when the d-band center is far from the Fermi level, the H* adsorption becomes weak. On the strain-free RuB_4, the ΔG_{H*}value on the Ru site is slightly negative (-8.8 meV), which indicates that the HER performance could be further improved if the d-band

center moves away from the Fermi level. The desired d-band center shifting (away from the Fermi level) can be achieved by exerting positive (tensile) strain (Fig. 5c): the strain at +2% can maximally enhance the HER activity. When the material is further stretched ($\varepsilon \geq +3\%$), the reduced value of the d-band center triggers a weaker interaction between Ru and H, and the ΔG_{H^*} for RuB_4 becomes slightly positive, as illustrated in Fig. 5b. In short, tuning d-band center can effectively modulate the adsorption/desorption of H and HER activity.

We then explored the hydrogen coverage (σ) effect on the HER catalytic performance. A unit cell of the RuB_4 monolayer containing four Ru and 16 B atoms was used in our studies. One H* adsorption on the basal plane of the layer corresponds to 1/20 coverage, and one to four hydrogen atoms adsorbed on the Ru sites were considered, corresponding to the hydrogen coverage of 1/20 to 4/20.The specific atomic adsorption sites are shown in Fig. S12 in ESI.As shown in Fig. 6a, the variation of ΔG_{H^*} (on the Ru sites) with increasing H coverage is evident. Still, the ΔG_{H^*} values fluctuate from -0.11 eV to 0.11 eV, indicating that the high HER acclivity of the RuB_4sheet is robust against H coverage.

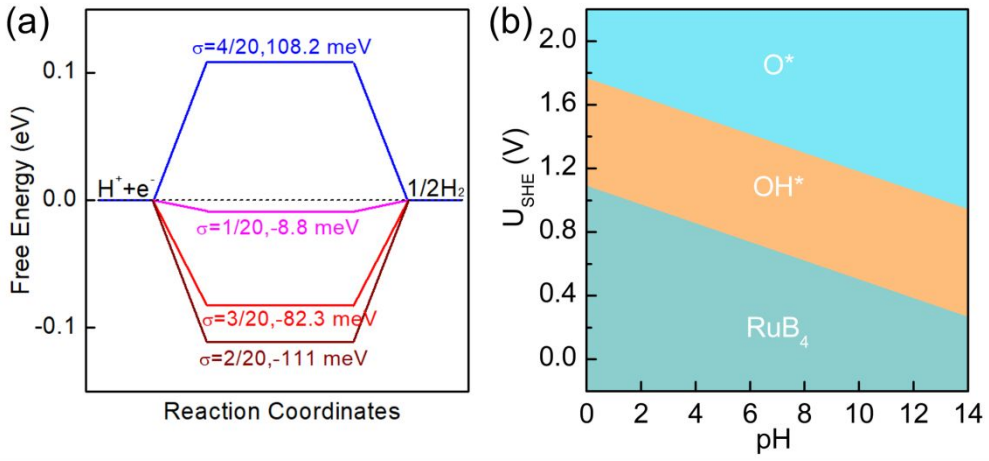

Fig. 6 (a) Gibbs free energy of H adsorption (ΔG_{H*}) on the Ru site of the RuB_4 monolayer at different hydrogen coverage (σ). (b) Surface Pourbaix diagram for the RuB_4 monolayer.

Lastly, to evaluate the stability of the RuB_4 monolayer in an aqueous electrochemical environment, we plotted its surface Pourbaix diagram (Fig. 6b) at the equilibrium.[65] The specific calculation details are presented in equations S1-S9 in the ESI. In an acidic solution at pH = 0, the RuB_4 sheet can be protected from oxidation by water when the U_{SHE} value is below 1.08 V. As the pH increases, lower potential energies are required to avoid oxidation with a slope of -0.059 V pH^{-1}. When the potential is more positive than the cathodic protection potential of the RuB_4 monolayer (e.g., U_{SHE} =1.08 V at pH=0), the RuB_4 sheet is oxidized and adsorbed by OH* (Fig. S13†). At even higher potentials, the OH* on RuB_4 can be further oxidized, forming the O*-covered RuB_4 sheet (e.g., U_{SHE} =1.76 V at pH=0). Clearly, under standard conditions (U_{SHE}=0), the bare RuB_4 sheet has good oxidation resistance, and the structure shows relatively high stability in the aqueous electrochemical environment, which is better than many other 2D catalysts, such as the MXene family[23] and WB_4sheet whose U_{SHE} displays negative values under the same conditions.[37]

4. Conclusions

In summary, we theoretically established that a 2D Dirac nodal loop semimetal, the RuB_4 monolayer, is a promising catalyst for enhanced HER performance. We found the RuB_4 monolayer exhibits superior stability, and its symmetry-protected nodal loop is robust against external strains. Especially, its basal plane, where the nodal loop presents, features rich HER active sites with a near-zero ΔG_{H*} value (-8.8

meV). Moreover, the 2D Dirac nodal loop quantum catalyst can provide high carrier densities with a stable supply of itinerant electrons at the active sites. All these unique characteristics endow the RuB_4 monolayer with great promise as a high-efficiency HER catalyst. Beyond identifying a new 2D HER catalyst, this work offers an innovative route to design catalysts by using the concept of Dirac nodal loop semimetals, which can be extended to many more nanomaterials and important electrocatalysts.

Author contributions

Y. J. and Z. C. conceptualization, investigation, validation, writing - review & editing, funding acquisition. F. M. resources, supervision, formal analysis, writing – original draft, funding acquisition. Z. G. investigation, formal analysis, visualization, data curation and writing - original draft. H. W. and Y. L. investigation. Y. G. and Z. Z. formal analysis (concerning symmetry analysis).

Conflicts of interest

The authors declare that they have no known competing financial interests or personal relationships that could have appeared to influence the work reported in this paper.

Acknowledgments

We thank Dr. G. Gao for the valuable discussions. This work is supported in China by the National Natural Science Foundation of China (Grant No. 11904077 and 12204144), the Natural Science Fund of Hebei Province for Excellent Young

Scientists Fund Program (Grant No. A2022205027), financial support program from Hebei Province (Grant No. E2019050018 and C20220503), Science Foundation of Hebei Normal University (Grant No. L2019B09), and the Key Program of Natural Science Foundation of Hebei Province (Grant No. A2021205024), and in the USA by the Department of Energy (Grant DE-SC0023418).

References

1. A. K. Hussein, *Renew. Sust. Energ. Rev.*, 2015, **42**, 460-476.
2. M. S. Dresselhaus and I. L. Thomas, *Nature*, 2001, **414**, 332-337.
3. G. W. Crabtree, M. S. Dresselhaus and M. V. Buchanan, *Phys. Today*, 2004, **57**, 39-44.
4. Y. Jiao, Y. Zheng, M. Jaroniec and S. Z. Qiao, *Chem. Soc. Rev.*, 2015, **44**, 2060-2086.
5. C. Huang, Y. Yu, J. Yang, Y. Yan, D. Wang, F. Hu, X. Wang, R. Zhang and G. Feng, *Applied Surface Science*, 2019, **476**, 928-936.
6. E. J. Popczun, C. G. Read, C. W. Roske, N. S. Lewis and R. E. Schaak, *Angew. Chem. Int. Ed.*, 2014, **53**, 5427-5430.
7. M. Wang, Z. Wang, X. Gong and Z. Guo, *Renew. Sust. Energ. Rev.*, 2014, **29**, 573-588.
8. J. Zhang, K. Sasaki, E. Sutter and R. R. Adzic, *Science*, 2007, **315**, 220-222.
9. R. Subbaraman, D. Tripkovic, D. Strmcnik, K. C. Chang, M. Uchimura, A. P. Paulikas, V. Stamenkovic and N. M. Markovic, *Science*, 2011, **334**, 1256-1260.
10. J. N. Tiwari, S. Sultan, C. W. Myung, T. Yoon, N. Li, M. Ha, A. M. Harzandi, H. J. Park, D. Y. Kim, S. S. Chandrasekaran, W. G. Lee, V. Vij, H. Kang, T. J. Shin, H. S. Shin, G. Lee, Z. Lee and K. S. Kim, *Nat. Energy*, 2018, **3**, 773-782.
11. G. Chen, T. Wang, J. Zhang, P. Liu, H. Sun, X. Zhuang, M. Chen and X. Feng, *Adv. Mater.*, 2018, **30**, 1706279.
12. M. Li, K. Duanmu, C. Wan, T. Cheng, L. Zhang, S. Dai, W. Chen, Z. Zhao, P. Li, H. Fei, Y. Zhu, R. Yu, J. Luo, K. Zang, Z. Lin, M. Ding, J. Huang, H. Sun, J. Guo, X. Pan, W. A. Goddard, P. Sautet, Y. Huang and X. Duan, *Nat. Catal*, 2019, **2**, 495-503.
13. S. T. Nguyen, L. K. Johnson, R. H. Grubbs and J. W. Ziller, *J. Am. Chem. Soc.*, 1992, **114**, 3974-3975.
14. X. Zhang, A. Chen, L. Chen and Z. Zhou, *Adv. Energy Mater*, 2022, **12**, 2003841.
15. Y. Ito, W. Cong, T. Fujita, Z. Tang and M. Chen, *Angew. Chem. Int. Ed.*

Engl., 2015, **54**, 2131-2136.
16. Y. Jia, L. Zhang, A. Du, G. Gao, J. Chen, X. Yan, C. L. Brown and X. Yao, 2016, **28**, 9532-9538.
17. C. Jin, L. Cheng, G. Feng, R. Ye, Z.-H. Lu, R. Zhang and X. Yu, *Langmuir*, 2022, **38**, 3694-3710.
18. A. B. Laursen, S. Kegnæs, S. Dahl and I. Chorkendorff, *Energy Environ. Sci.*, 2012, **5**, 5577-5591.
19. C. G. Morales-Guio and X. Hu, *Acc. Chem. Res.*, 2014, **47**, 2671-2681.
20. D. Merki and X. Hu, *Energy Environ. Sci.*, 2011, **4**, 3878-3888.
21. D. Voiry, H. Yamaguchi, J. Li, R. Silva, D. C. B. Alves, T. Fujita, M. Chen, T. Asefa, V. B. Shenoy, G. Eda and M. Chhowalla, *Nat. Mater.*, 2013, **12**, 850-855.
22. L. Cheng, W. Huang, Q. Gong, C. Liu, Z. Liu, Y. Li and H. Dai, *Angew. Chem. Int. Ed.*, 2014, **53**, 7860-7863.
23. G. Gao, A. P. O'Mullane and A. Du, *ACS Catal.*, 2017, **7**, 494-500.
24. H. Liu, K. Hu, D. Yan, R. Chen, Y. Zou, H. Liu and S. Wang, *Adv. Mater.*, 2018, **30**, 1800295.
25. S. Chandrasekaran, D. Ma, Y. Ge, L. Deng, C. Bowen, J. Roscow, Y. Zhang, Z. Lin, R. D. K. Misra, J. Li, P. Zhang and H. Zhang, *Nano Energy*, 2020, **77**, 105080.
26. T. Tang, Z. Wang and J. Guan, *Chinese J. Catal*, 2022, **43**, 636-678.
27. F. Jaramillo Thomas, P. Jørgensen Kristina, J. Bonde, H. Nielsen Jane, S. Horch and I. Chorkendorff, *Science*, 2007, **317**, 100-102.
28. I. Karunadasa Hemamala, E. Montalvo, Y. Sun, M. Majda, R. Long Jeffrey and J. Chang Christopher, *Science*, 2012, **335**, 698-702.
29. R. Xie, T. Zhang, H. Weng and G.-L. Chai, *Small Sci.*, 2022, **2**, 2100106.
30. N. Meinzer, *Nat. Rev. Mater*, 2017, **2**, 17021.
31. C. R. Rajamathi, U. Gupta, N. Kumar, H. Yang, Y. Sun, V. Süß, C. Shekhar, M. Schmidt, H. Blumtritt, P. Werner, B. Yan, S. Parkin, C. Felser and C. N. R. Rao, *Adv. Mater.*, 2017, **29**, 1606202.
32. G. Li, C. Fu, W. Shi, L. Jiao, J. Wu, Q. Yang, R. Saha, M. E. Kamminga, A. K. Srivastava, E. Liu, A. N. Yazdani, N. Kumar, J. Zhang, G. R. Blake, X. Liu, M. Fahlman, S. Wirth, G. Auffermann, J. Gooth, S. Parkin, V. Madhavan, X. Feng, Y. Sun and C. Felser, *Angew. Chem. Int. Ed. Engl.*, 2019, **58**, 13107-13112.
33. J. Li, H. Ma, Q. Xie, S. Feng, S. Ullah, R. Li, J. Dong, D. Li, Y. Li and X.-Q. Chen, *Sci. China Mater*, 2018, **61**, 23-29.
34. L. Li, J. Zeng, W. Qin, P. Cui and Z. Zhang, *Nano Energy*, 2019, **58**, 40-46.
35. Q. Qu, B. Liu, J. Liang, H. Li, J. Wang, D. Pan and I. K. Sou, *ACS Catal.*, 2020, **10**, 2656-2666.
36. L. Wang, X. Zhang, W. Meng, Y. Liu, X. Dai and G. Liu, *J. Mater. Chem. A*, 2021, **9**, 22453-22461.
37. A. Wang, L. Shen, M. Zhao, J. Wang, W. Zhou, W. Li, Y. Feng and H. Liu, *J. Mater. Chem. C*, 2019, **7**, 8868-8873.

38. G. Kresse and J. Furthmüller, *Phys. Rev. B*, 1996, **54**, 11169-11186.
39. P. E. Blöchl, *Phys. Rev. B*, 1994, **50**, 17953-17979.
40. J. P. Perdew, K. Burke and M. Ernzerhof, *Phys. Rev. Lett.*, 1996, **77**, 3865-3868.
41. M. Sun, Q. Ren, Y. Zhao, J.-P. Chou, J. Yu and W. Tang, *Carbon*, 2017, **120**, 265-273.
42. V. I. Anisimov, J. Zaanen and O. K. Andersen, *Physical Review B*, 1991, **44**, 943-954.
43. A. Togo, F. Oba and I. Tanaka, *Phys. Rev. B*, 2008, **78**, 134106.
44. S. Baroni, S. de Gironcoli, A. Dal Corso and P. Giannozzi, *Rev. Mod. Phys.*, 2001, **73**, 515-562.
45. J. K. Nørskov, T. Bligaard, A. Logadottir, J. R. Kitchin, J. G. Chen, S. Pandelov and U. Stimming, *Journal of The Electrochemical Society*, 2005, **152**, J23.
46. B. E. Conway and J. O. m. Bockris, *J. Chem. Phys.*, 1957, **26**, 532-541.
47. R. Parsons, *Trans. Faraday Society*, 1958, **54**, 1053-1063.
48. H. Zhang, Y. Li, J. Hou, A. Du and Z. Chen, *Nano Lett.*, 2016, **16**, 6124-6129.
49. C. Tang, K. Ostrikov, S. Sanvito and A. Du, *Nanoscale Horiz.*, 2021, **6**, 43-48.
50. H. Zhang, Y. Li, J. Hou, K. tu and Z. Chen, *J. Am. Chem. Soc.*, 2016, **138**.
51. Z.-j. Wu, E.-j. Zhao, H.-p. Xiang, X.-f. Hao, X.-j. Liu and J. Meng, *Phys. Rev. B*, 2007, **76**, 054115.
52. C. Zhang, Y. Jiao, F. Ma, S. Bottle, M. Zhao, Z. Chen and A. Du, *Phys. Chem. Chem. Phys.*, 2017, **19**, 5449-5453.
53. P. E. Trevisanutto, C. Giorgetti, L. Reining, M. Ladisa and V. Olevano, *Phys. Rev. Lett.*, 2008, **101**, 226405.
54. B. Wang, S. J. Yuan, Y. H. Li, L. Shi and J. L. Wang, *Nanoscale*, 2017, **9**, 5577-5582.
55. L. Z. Zhang, Z. F. Wang, S. X. Du, H. J. Gao and F. Liu, *Phys. Rev. B*, 2014, **90**, 161402.
56. F. Ma, Y. Jiao, G. Gao, Y. Gu, A. Bilic, Z. Chen and A. Du, *Nano Lett.*, 2016, **16**, 3022-3028.
57. Z. Liu, R. Lou, P. Guo, Q. Wang, S. Sun, C. Li, S. Thirupathaiah, A. Fedorov, D. Shen, K. Liu, H. Lei and S. Wang, *Physical Review X*, 2018, **8**, 031044.
58. X.-B. Wang, X.-M. Ma, E. Emmanouilidou, B. Shen, C.-H. Hsu, C.-S. Zhou, Y. Zuo, R.-R. Song, S.-Y. Xu, G. Wang, L. Huang, N. Ni and C. Liu, *Phys. Rev. B*, 2017, **96**, 161112.
59. M. M. Hosen, K. Dimitri, I. Belopolski, P. Maldonado, R. Sankar, N. Dhakal, G. Dhakal, T. Cole, P. M. Oppeneer, D. Kaczorowski, F. Chou, M. Z. Hasan, T. Durakiewicz and M. Neupane, *Phys. Rev. B*, 2017, **95**, 161101.
60. J.-S. Li, Y. Wang, C.-H. Liu, S.-L. Li, Y.-G. Wang, L.-Z. Dong, Z.-H. Dai, Y.-F. Li and Y.-Q. Lan, *Nat. Commun.*, 2016, **7**, 11204.
61. Y. Zheng, Y. Jiao, Y. Zhu, L. H. Li, Y. Han, Y. Chen, A. Du, M. Jaroniec and S. Z. Qiao, *Nat. Commun.*, 2014, **5**, 3783.
62. D. Wang, Z.-P. Liu and W.-M. Yang, *ACS Catal.*, 2018, **8**, 7270-7278.

63. J. Deng, P. Ren, D. Deng and X. Bao, *Angew. Chem. Int. Ed.*, 2015, **54**, 2100-2104.
64. Y. Zheng, Y. Jiao, M. Jaroniec and S. Z. Qiao, *Angew. Chem. Int. Ed.*, 2015, **54**, 52-65.
65. H. A. Hansen, J. Rossmeisl and J. K. Nørskov, *Physical Chemistry Chemical Physics*, 2008, **10**, 3722-3730.